Probabilistic Engineering Mechanics 57 (2019) 1–13

Contents lists available at ScienceDirect

Probabilistic Engineering Mechanics

journal homepage: www.elsevier.com/locate/probengmech

Distribution tail structure and extreme value analysis of constrained piecewise linear oscillators

Vadim Belenky [a,*], Dylan Glotzer [d], Vladas Pipiras [b], Themistoklis P. Sapsis [c]

[a] Naval Surface Warfare Center Carderock Division, United States
[b] The University of North Carolina at Chapel Hill, United States
[c] Massachusetts Institute of Technology, United States
[d] Meredith College, United States

ARTICLE INFO

Keywords:
Linear and nonlinear oscillators
White noise and correlated excitations
Piecewise linear restoring force (stiffness)
Distribution tails
Fokker–Planck–Kolmogorov equation
Generalized Pareto distribution
Ship roll motion

ABSTRACT

A single-degree-of-freedom random oscillator with a piecewise linear restoring force (experiencing softening after a certain point value of the response, called a "knuckle" point) is studied with the goal of understanding the structure of the distribution tail of its response or (local) maximum. A theoretical analysis is carried out by two approaches: first, by focusing on the maximum and response after crossing the "knuckle" point, where explicit calculations can be performed assuming standard distributions for the derivative at the crossing, and second, by considering the white noise random external excitation, where the stationary distribution of the response is readily available from the literature. Both approaches reveal the structure of the distribution tails where a Gaussian core is followed by a heavier tail, possibly having a power-law form, which ultimately turns into a tail having a finite upper bound (referred to as a light tail). The extent of the light tail region is also investigated, and shown to be the result of the conditioning for the system not to reach the unstable equilibrium. The study is motivated by applications to ship motions, where the considered random oscillator serves as a prototypical model for ship roll motion in beam seas, and estimation of the probabilities of these motions exceeding large critical angles is of interest. Standard statistical methodology for such estimation is based on the peaks-over-threshold approach, for which several lessons are drawn from the analysis of the tail structure of the considered random oscillator.

1. Introduction

Piecewise linear oscillators might seem to be exotic models for engineering applications as most of the real-world forces are smooth. Nevertheless, they have proved useful on several occasions, e.g. as in the classical problem of a dynamical system with dry friction [1]. Another application area concerning ship motions will be discussed in more detail below. Thus, consider a single-degree-of-freedom random oscillator given by

$$\ddot{x} + 2\delta\dot{x} + r(x) = y(t), \tag{1.1}$$

where $\delta > 0$ is a damping parameter, $r(x) = \nabla V(x)$ is a nonlinear restoring force (stiffness) associated with a potential function V and $y(t)$ is an external random excitation (forcing). The potential function is characterized by the existence of a stable center and two symmetric unstable saddle equilibrium points. The stiffness function associated with such potential is assumed to have a piecewise linear form given by

$$r(x) = \begin{cases} -k_1\omega_0^2\left(x + x_m\right) - \omega_0^2 x_m, & \text{if } x < -x_m, \\ \omega_0^2 x, & \text{if } -x_m \le x \le x_m, \\ -k_1\omega_0^2\left(x - x_m\right) + \omega_0^2 x_m, & \text{if } x > x_m, \end{cases} \tag{1.2}$$

where ω_0 is a natural frequency in the linear regime $(-x_m, x_m)$, $-k_1\omega_0^2 < 0$ is a negative slope in the nonlinear regime $|x| > x_m$ and x_m, called the "knuckle" point, defines the threshold above which the system behaves nonlinearly, i.e. the point above which the restoring force is decreasing. The corresponding potential for this case is given by

$$V(x) = \begin{cases} -\frac{1}{2}k_1\omega_0^2 x^2 - \left(k_1+1\right)\omega_0^2 x_m x - \frac{1}{2}\left(k_1+1\right)\omega_0^2 x_m^2, & \text{if } x < -x_m, \\ \frac{1}{2}\omega_0^2 x^2, & \text{if } -x_m \le x \le x_m, \\ -\frac{1}{2}k_1\omega_0^2 x^2 + \left(k_1+1\right)\omega_0^2 x_m x - \frac{1}{2}\left(k_1+1\right)\omega_0^2 x_m^2, & \text{if } x > x_m. \end{cases} \tag{1.3}$$

Fig. 1 provides the plots of a generic piecewise linear stiffness function (1.2), the associated potential function (1.3) and the phase space (for the unforced, unperturbed system). The point $x_v > 0$ such that $r(x_v) = 0$ corresponding to the unstable equilibrium is referred to as the point of vanishing stability, and will play an important role below.

* Corresponding author.
E-mail address: vadim.belenky@navy.mil (V. Belenky).

https://doi.org/10.1016/j.probengmech.2019.04.001
Received 14 April 2018; Received in revised form 13 January 2019; Accepted 8 April 2019
Available online 22 April 2019
0266-8920/Published by Elsevier Ltd.

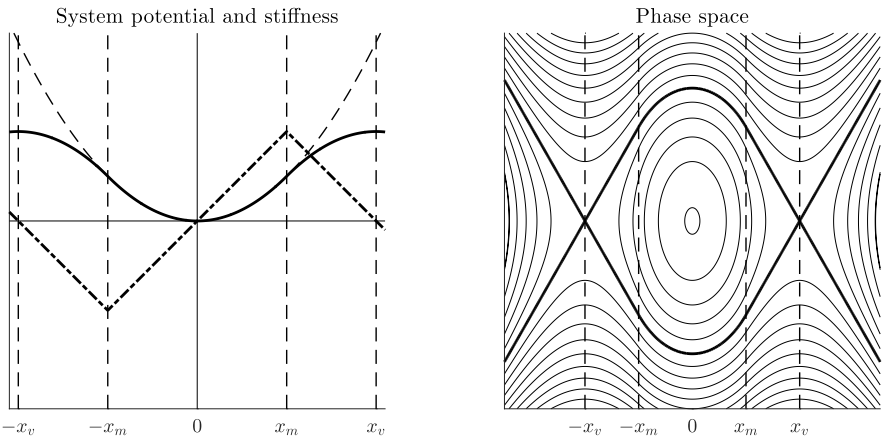

Fig. 1. Left: a piecewise linear stiffness function $r(x)$ (dash-dotted curve) and its associated potential function $V(x)$ (solid curve). The potential function for the linear stiffness function is also shown (dashed curve), as are $-x_m$, x_m, $-x_v$, x_v (dashed vertical lines). Right: A phase portrait of the system on the left.

The model (1.1)–(1.3) is an attractive tool for a qualitative consideration of large roll motions of a ship in waves, including capsizing (understanding the latter as a transition to motion near another stable equilibrium). Indeed, the piecewise linear function (1.2) is a schematic model of an actual ship roll stiffness resulting from hydrostatic and hydrodynamic pressures over the submerged portion of the ship hull. While this model can be seen as a very simplistic one, it retains most known nonlinear properties of an oscillator with a similar smooth stiffness, including loss of isochronism, fold and flip bifurcations, as well as fractalization of the safe basin [2]. It also allows for a closed-form solution to the probability of capsizing within a given time [3]. The model has seen some further development and applications, e.g. by Paroka and Umeda [4]. Another important outcome of the study of piecewise linear oscillators was the so-called "split-time" approach to find the probability of capsizing by a novel numerical simulation scheme; see [5] for a review. This reference also contains an updated and rectified closed-form solution for capsizing with a piecewise linear stiffness.

Ship stability accidents are not limited to capsizing. Encountering large (extreme) roll angles can also have catastrophic impact, in terms of both human, cargo or machinery loss. Indeed, probabilistic characterization of extreme values of ship roll has attracted much attention in Naval Architecture. A Weibull distribution is employed for wave loads, e.g. for vertical bending moment [6]. Significant nonlinearity of roll motion, however, prevents this conventional approach for probabilistic characterization of dynamic stability. Some of the approaches, accounting for nonlinearity of roll motions, have been reviewed in [7]. Recent works include further development of the critical wave group method by Malara et al. [8], Anastopoulos et al. [9], and path integration method by Kougioumtzoglou and Spanos [10], Chai et al. [11]. Modern simulation tools for probabilistic characterization are reviewed in [12]. See also [13] who focus specifically on accreditation for regulatory applications.

Another standard statistical approach to characterizing extremes is the peaks-over-threshold (POT) method based on fitting a generalized Pareto distribution (GPD) to data above a suitably chosen threshold (e.g. [14–16]). The POT approach has been applied to ship motions and loads data (e.g. [17–20]) and has generally been found to perform well in characterizing extremes. The GPD density is expressed as

$$f_{\mu,\xi,\sigma}(x) = \begin{cases} \frac{1}{\sigma}\left(1+\frac{\xi(x-\mu)}{\sigma}\right)^{-1/\xi-1}, & \mu < x, \quad \text{if } \xi > 0, \\ \frac{1}{\sigma}e^{-\frac{x-\mu}{\sigma}}, & \mu < x, \quad \text{if } \xi = 0, \\ \frac{1}{\sigma}\left(1+\frac{\xi(x-\mu)}{\sigma}\right)^{-1/\xi-1}, & \mu < x < \mu - \frac{\sigma}{\xi}, \quad \text{if } \xi < 0, \end{cases} \tag{1.4}$$

where ξ is the *shape* parameter, σ is the *scale* parameter and μ is a *threshold*. The GPD has an upper bound $(-\sigma/\xi)$ (above the threshold) for a negative shape parameter $\xi < 0$. This case shall be referred to as that of a light tail. When $\xi = 0$, the GPD is the usual exponential distribution. When $\xi > 0$, on the other hand, the GPD density has a power-law tail behavior $Cx^{-1/\xi-1}$ with constant $C > 0$ and exponent $-1/\xi - 1$. In this case, the tail is heavy, especially compared to the tail of a Gaussian distribution. Unless specified otherwise, a heavy tail will refer to a distribution tail that is heavier than that of a normal distribution, and the term "power-law tail" or "power-law heavy tail" will refer to the tail behavior $Cx^{-1/\xi-1}$ with $\xi > 0$.

The GPD is an asymptotic distribution, while ship roll data arise as a response of a strongly nonlinear dynamical system. The available data does not necessarily provide sufficient information about the system, and the approximation of the tail with GPD may not necessarily reflect real limiting behavior of the nonlinear system. For example, if the available data on the response of the system (1.1) does not include any transitions to another stable equilibrium (capsizing), the POT method will not be able to predict it, unless some additional information is provided. Thus, the solution has to be sought in complementing statistical analysis of the response with mathematical models reflecting physics of particular nonlinear dynamical systems.

A practical step towards this objective is to try to relate a character of nonlinearity and a type of statistical estimate of the response. Belenky and Sevastianov [21] described an influence of the initial form of the roll stiffness on the deviation of roll distribution from normal. Mohamad and Sapsis [22] and Mohamad et al. [23] introduced a probabilistic decomposition method to describe the influence of instabilities on the heavy-tailed statistics of general dynamical systems. Consideration of an intermittent resonance allows applying this approach to parametric roll [24], where it successfully reproduces a shape of a distribution observed in high-fidelity numerical simulation [25]. Another example is the introduction of a limiting upper bound to pitch motions [20], reflecting the fact that a ship loses sensitivity to wave excitation once pitch angle exceeds a certain value. The result is a dramatic shrinkage of confidence intervals, i.e. the statistical uncertainty of an extrapolated estimate is decreased by introducing additional physical information.

The goals of this study are, in broad terms, to examine the properties of the distribution and its tail of the response (and local maxima) of the piecewise linear oscillator, to interpret them from a physical standpoint whenever possible, and to understand their implications for available extreme value techniques such as the POT approach. A more concrete question of interest, for example, is why [18,19] systematically observed positive shape parameters while fitting GPD to the roll peak data. At first glance, a negative shape parameter and the distribution having an upper bound might be expected: observing a roll

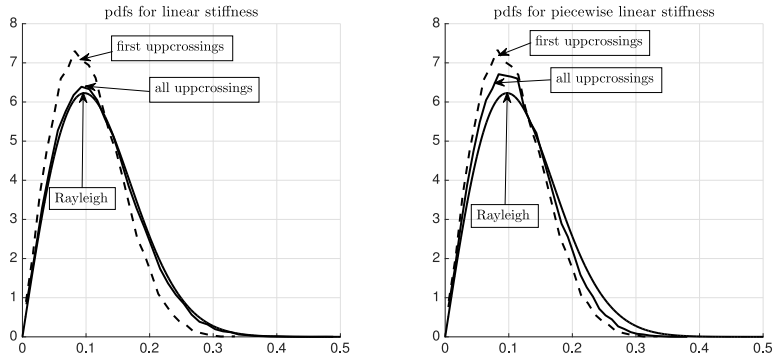

Fig. 2. Left: The empirical pdfs of $\dot{x}(t)$ from 30,000 h at the upcrossing of x_m for all upcrossings (dashed curve) and the first upcrossings (solid curve) per 30-min record. Also, the Rayleigh pdf with parameter $\sigma_{\dot{x}} = 0.13$ rad/s (solid smooth curve) is plotted. Right: The same empirical pdfs of $\dot{x}(t)$ calculated for a piecewise linear system with the same Rayleigh distribution.

peak means a ship returning to its stable equilibrium, and a limit is expected beyond which a ship would not return (i.e. she will capsize).

The goals above are achieved by deriving and interpreting the distribution of the response (and local maxima) of the piecewise linear oscillator in two complementary approaches: the first approach for correlated excitation by taking advantage of the piecewise linear form of the stiffness (see Section 2 below), and the second approach for white noise excitation based on the Fokker–Planck–Kolmogorov equation (see Section 3 below). Both approaches reveal the structure of the distribution tails where a Gaussian core is followed by a heavier tail, possibly power-law heavy, which ultimately turns into a light tail with a finite upper bound. Some implications of the findings on extreme value analysis using GPD are also discussed (Section 4 below). The study ends with a summary and conclusions (Section 5 below), and an appendix is included with details on the synthetic processes employed in this work. The paper extends earlier study by the authors [26].

2. Probabilistic response for system with piecewise linear stiffness and correlated Gaussian excitation

The focus here is on the distributions of the response of the oscillator (1.1)–(1.2) and its largest values (local maxima). Excitation is assumed to be a stationary ergodic correlated Gaussian process. The consideration is limited to the values exceeding the "knuckle" point $x > x_m$. As the slope of the piecewise linear stiffness is negative for $x \in [x_m, x_v]$, the excitation may be "switched off" for $x > x_m$. This assumption is based on the notion that lightly-damped dynamical systems receive most of their energy for the excitation through the resonance, while the latter is not possible when the slope of stiffness is negative [21].

2.1. Solution in the nonlinear regime and the case of absent excitation

When the excitation is switched off above the "knuckle" point, the solution of (1.1) above the "knuckle" point $x > x_m$ is given by

$$x(t) = Ae^{\lambda_1 t} + Be^{\lambda_2 t} + x_v, \tag{2.1}$$

where

$$\lambda_1 = -\delta + \sqrt{k_1 w_0^2 + \delta^2} > 0, \quad \lambda_2 = -\delta - \sqrt{k_1 w_0^2 + \delta^2} < 0 \tag{2.2}$$

are the two eigenvalues associated with the linear oscillator (1.1) in the regime $x > x_m$, and A, B are constants determined by the initial conditions $x_m, \dot{x}_1$ of $x, \dot{x}$ at the upcrossing of x_m by x, through

$$A = \frac{\dot{x}_1 + \lambda_2(x_v - x_m)}{\lambda_1 - \lambda_2}, \quad B = -\frac{\lambda_1(x_v - x_m) + \dot{x}_1}{\lambda_1 - \lambda_2}. \tag{2.3}$$

The absence of capsizing now corresponds to the case $A < 0$ (see also [3]), and hence $\dot{x}_1 < \dot{x}_{\rm cr}$ with the critical value of the derivative at the upcrossing given by

$$\dot{x}_{\rm cr} = -\lambda_2(x_v - x_m). \tag{2.4}$$

The constant B is always negative.

If no capsizing occurs, the solution (2.1) can also be expressed through the hyperbolic cosine as

$$x(t) = He^{-\delta t}\cosh(\omega_1 t + \epsilon) + x_v, \tag{2.5}$$

where $\omega_1 = \sqrt{k_1 w_0^2 + \delta^2}$, and the "magnitude" H and the "phase" ϵ are constants defined as

$$H = -\frac{1}{\omega_1}\sqrt{\omega_1^2(x_m - x_v)^2 - (\dot{x}_1 + \delta(x_m - x_v))^2}, \tag{2.6}$$

$$\epsilon = \tanh^{-1}\Big(\frac{\dot{x}_1 + \delta(x_m - x_v)}{\omega_1(x_m - x_v)}\Big). \tag{2.7}$$

For stationary Gaussian excitations, the probability density function (pdf) of the derivative $\dot{x}_1$ at the upcrossing is expected to be approximated by a Rayleigh distribution with density

$$\frac{z}{\sigma_{\dot{x}}^2} e^{-z^2/2\sigma_{\dot{x}}^2}, \quad z > 0, \tag{2.8}$$

where $\sigma_{\dot{x}}^2 = \mathbb{E}\dot{x}_l(0)^2$ and $x_l(t)$ is the solution of (1.1) supposing the stiffness function of the linear regime throughout the whole domain. Indeed, recall that Eq. (2.8) describes the pdf of a value of the first derivative of a stationary Gaussian process taken at the instant of upcrossing of a given level (for example, [27], p. 201; [28], Section 8.4; [29], pp. 161–162; [5], Section 2.4). Supposing $A < 0$, the density of $\dot{x}_1$ can then be thought of as

$$f_{\dot{x}_1}(z) = \frac{ze^{-z^2/2\sigma_{\dot{x}}^2}}{\sigma_{\dot{x}}^2(1 - e^{-\dot{x}_{\rm cr}^2/2\sigma_{\dot{x}}^2})}, \quad 0 < z < \dot{x}_{\rm cr}. \tag{2.9}$$

In fact, some caution needs to be exercised in using (2.8) for the purposes here. The pdf (2.8) is that of the derivative $\dot{x}_1$ at an upcrossing of a linear system, but this includes *all* upcrossings. A response of the dynamical system is correlated, and one upcrossing is often followed by another upcrossing, so that they appear in clusters. Consider the first upcrossing in each cluster as a way to sample independent upcrossings. Then, the pdf of these independent upcrossings might, in fact, be different from that in (2.8) for all upcrossings. Comparison between an empirical pdf of the first upcrossings and the pdf of all upcrossings is shown in the left plot of Fig. 2. (The system parameters are given at the end of this section.) A good agreement is obtained with (2.8) in the case of all upcrossings but *not* in the case of first upcrossings. The value of the derivative at an upcrossing is related to the value of the peak to follow this upcrossing. The higher peak comes with a larger derivative at the preceding upcrossing. The first peak (the derivative at the first upcrossing, respectively) is not usually the largest in a cluster, and the average first peak (the average derivative at the first upcrossing, respectively) in a cluster will not necessarily be equal to the average of all peaks (derivatives, respectively) above the upcrossing threshold. In fact, Fig. 2, left plot, suggests that the derivatives at the first upcrossings are smaller on average than the derivatives at all upcrossings.

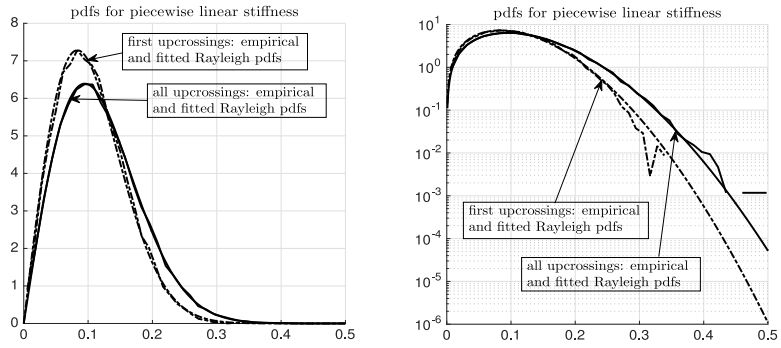

Fig. 3. Left: The empirical pdfs of $\dot{x}(t)$ and their fitted Rayleigh pdfs. For all upcrossings (solid curves), the fitted Rayleigh parameter is $\hat{\sigma}_{\dot{x}} = 0.089$ rad/s; for the first upcrossings, it is 0.084 rad/s. Right: The same plot on a vertical log scale.

The right plot of Fig. 2 shows similar quantities for the piecewise linear system. The empirical pdf of the derivatives at all upcrossings is no longer in agreement with the theoretical pdf in (2.8). Each time the "knuckle" point is crossed, the oscillations (2.1) with natural frequency are generated. If the piecewise linear system is lightly damped for $x \in [-x_m, x_m]$, the oscillations do not die out until the next crossing. As a result, the value of the derivative at the upcrossing is altered compared to the linear system (where the oscillations with natural frequency are present only at the initial transition).

Though no agreement is observed with (2.8) in the right plot of Fig. 2, the Rayleigh distribution still provides a good fit to the two empirical distributions of that figure. This is illustrated in Fig. 3. Its left plot shows the two Rayleigh fits (for the Rayleigh parameters $\sigma^2_{\dot{x}}$ in (2.8) chosen through maximum likelihood). The right plot shows the same plot but on the vertical log scale, where a slight disagreement can be seen in the tails of the empirical and fitted distributions for first upcrossings — the empirical pdf seems slightly lighter in the tail than the Rayleigh distribution. Since the Rayleigh fits are generally satisfactory in Fig. 3, the pdf of the derivative at the upcrossing in the case of the piecewise linear system will still be assumed as (2.8), with the understanding that its parameter $\sigma^2_{\dot{x}}$ may need to be adjusted.

The excitation process $y(t)$ and other parameters used in simulations throughout the paper are defined as follows. The process $y(t)$ is assumed to be a zero mean Gaussian process with the spectral density given and discussed in Appendix. The plots in Figs. 2 and 3 correspond to the significant wave height $H_s = 9$ m and the mean period $T_1 = 11.595$ s. The other parameter values in the system (1.1)–(1.2) are the damping parameter δ, the natural frequency ω_0, the "knuckle" point x_m, and the slope parameter k_1. For Figs. 2 and 3, these are $\omega_0 = 0.6$ rad/s, $\delta = 0.15\omega_0$, $x_m = \pi/6 = 0.5236$ rad and $k_1 = 1$ but may change in other simulations below.

2.2. The distribution of the maximum value

The solution (2.1) depends on only one random variable: the derivative value at upcrossing $\dot{x}_1$ with its distribution described by (2.8). Thus, the expression (2.1) can be seen as a deterministic function of a random variable. Consider the distribution of the maximum value of (2.1) first, as its derivation is easier than the distribution of all the points in the solution (2.1). In the absence of capsizing ($A < 0$), the time of maximum of (2.1) can be found by setting the derivative of (2.1) to zero, which results in:

$$t_{\max} = \frac{1}{\lambda_1 - \lambda_2} \log\Big(-\frac{\lambda_2 B}{\lambda_1 A}\Big). \tag{2.10}$$

A zero value of the derivative of (2.1) at $t_{\max}$ allows expressing the constant B as $B = -(\lambda_1/\lambda_2)Ae^{(\lambda_1-\lambda_2)t_{\max}}$, which leads the following formula for the maximum value:

$$x_{\max} = x(t_{\max}) = x_v - \Big(1 - \frac{\lambda_1}{\lambda_2}\Big)\Big(-\frac{\lambda_2}{\lambda_1}\Big)^{\frac{\lambda_1}{\lambda_1-\lambda_2}} |B|^{\frac{\lambda_1}{\lambda_1-\lambda_2}} |A|^{-\frac{\lambda_2}{\lambda_1-\lambda_2}} =: G(\dot{x}_1), \tag{2.11}$$

where $x_m < G(\dot{x}_1) < x_v$ for $0 < \dot{x}_1 < \dot{x}_{\text{cr}}$. The density of the maximum value (2.11) is then given by

$$f_{x_{\max}}(x) = f_{\dot{x}_1}(G^{-1}(x)) \Big|\frac{d}{dx} G^{-1}(x)\Big|, \quad x_m < x < x_v. \tag{2.12}$$

The function G in (2.11) does not have an inverse expressible in closed form so that the density (2.12) cannot be written in closed form either. The structure of the density can nevertheless be explored in at least two ways: its tail around the unstable equilibrium/endpoint x_v, and its form in the special case of no damping when $\delta = 0$ (above x_m).

2.2.1. Behavior of the density around unstable equilibrium

Consider the situation just short of capsizing, i.e. the solution (2.1) when the value of the derivative at the upcrossing is just slightly below the critical value (2.4):

$$\dot{x}_1 = \dot{x}_{\text{cr}} - \Delta\dot{x}, \tag{2.13}$$

where $\Delta\dot{x}$ is small. The constants A and B can be expressed in terms of $\Delta\dot{x}$ as

$$A = \frac{\Delta\dot{x}}{\lambda_1 - \lambda_2}, \quad B = \frac{\Delta\dot{x}}{\lambda_1 - \lambda_2} - (x_v - x_m) \approx -(x_v - x_m). \tag{2.14}$$

Substitution of (2.13) and (2.14) into (2.11) yields the approximation of the distribution of the maximum near capsizing, i.e. at the tail: as $\dot{x}_1 \uparrow \dot{x}_{\text{cr}}$ (or $\Delta\dot{x} \downarrow 0$),

$$G(\dot{x}_1) \approx x_v - C_0(\dot{x}_{\text{cr}} - \dot{x}_1)^{-\frac{\lambda_2}{\lambda_1-\lambda_2}}, \tag{2.15}$$

where

$$C_0 = \Big(1 - \frac{\lambda_1}{\lambda_2}\Big)\Big(\frac{\lambda_2}{\lambda_1}(x_m - x_v)\Big)^{\frac{\lambda_1}{\lambda_1-\lambda_2}} (\lambda_1 - \lambda_2)^{\frac{\lambda_2}{\lambda_1-\lambda_2}}. \tag{2.16}$$

The function (2.15) can be inverted in closed form: as $x \uparrow x_v$,

$$G^{-1}(x) \approx \dot{x}_{\text{cr}} - \Big(\frac{x_v - x}{C_0}\Big)^{-\frac{\lambda_1-\lambda_2}{\lambda_2}} \tag{2.17}$$

and hence

$$f_{x_{\max}}(x) \approx \frac{(\lambda_1 - \lambda_2) f_{\dot{x}_1}(\dot{x}_{\text{cr}})}{(-\lambda_2) C_0^{-(\lambda_1-\lambda_2)/\lambda_2}} (x_v - x)^{-\frac{\lambda_1-\lambda_2}{\lambda_2}-1} = C_1 (x_v - x)^{-\frac{\lambda_1-\lambda_2}{\lambda_2}-1}. \tag{2.18}$$

Analysis of the tail structure based on the formula (2.18) is further discussed below.

2.2.2. Special case of no damping

The oscillator (1.1)–(1.2) is only an approximate qualitative model of large ship rolling. While the roll damping actually increases at large roll angles because sharp edges of deck structures enter water, for the purposes of the present analysis, this can be neglected. The topology of the phase plane is defined by the shape of stiffness. Also, the shape of the distribution near the mean value is mostly defined by the initial shape of stiffness [21], so that the shape of the tail is also influenced by the stiffness more than by the damping.

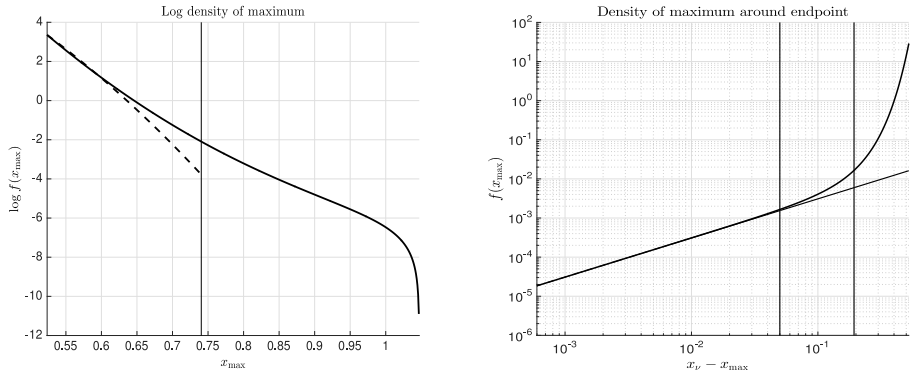

Fig. 4. Left: The density $f(x_{\max})$ of the maximum value on the log vertical scale. Right: The density $f(x_{\max})$ around the endpoint x_v on the log–log scale.

In the case of no damping $\delta = 0$, the functions G, G^{-1} and the density $f_{x_{\max}}$ can be expressed in closed form. Use of the hyperbolic form of the solution (2.5) is more convenient here. When $\delta = 0$, $\omega_1 = \sqrt{k_1}\omega_0$ and hence

$$x(t) = H\cosh(\omega_1 t + \epsilon) + x_v, \tag{2.19}$$

where the magnitude and the phase shift are

$$H = -\frac{1}{\omega_1}\sqrt{\omega_1^2(x_m - x_v)^2 - \dot{x}_1^2}, \quad \epsilon = \tanh^{-1}\Big(\frac{\dot{x}_1}{\omega_1(x_m - x_v)}\Big). \tag{2.20}$$

The maximum value is then

$$x_{\max} = x_v + H =: G(\dot{x}_1) \tag{2.21}$$

and hence

$$G^{-1}(x) = \omega_1\sqrt{(x_v - x_m)^2 - (x_v - x)^2}, \quad x_m < x < x_v. \tag{2.22}$$

Substituting (2.22) into (2.12) and using (2.9) leads to the density of the maximum value (2.21) given by

$$f_{x_{\max}}(x) = C(x_v - x)e^{\frac{\omega_1^2}{2\sigma_{\dot{x}}^2}(x_v - x)^2}, \quad x_m < x < x_v, \tag{2.23}$$

where

$$C^{-1} = \frac{\sigma_{\dot{x}}^2}{\omega_1^2}(e^{\frac{\omega_1^2}{2\sigma_{\dot{x}}^2}(x_v - x_m)^2} - 1)$$

is a normalizing constant. Since $(\lambda_1 - \lambda_2)/\lambda_2 = -2$ in the case of no damping, the form (2.23) is consistent with (2.18) as $x \uparrow x_v$.

2.2.3. Tail without damping

The left plot, solid line, of Fig. 4 depicts the density (2.23) on the log vertical scale, for the parameter values $\delta = 0$, $\sigma_{\dot{x}}^2 = 0.0066$, $x_m = \pi/6$, $x_v = \pi/3$, $w_0 = 0.6$ and $k_1 = 1$, which are typical values for ship dynamics. For comparison, the density (in dashed line) of the maximum value for the corresponding linear system is also included, supposing that the derivative at the upcrossing is smaller than $\dot{x}_{\text{cr}}$ in (2.4). (The calculation of the distribution in this case is similar to that above and is omitted.) The density (2.23) has a heavier tail than that of the linear system before collapsing at the endpoint x_v. At the same time, the right upper bound of the distribution is evident around $x_v = \pi/3$.

The right plot of Fig. 4 depicts the same density (2.23) on the log–log scale around the unstable equilibrium/endpoint x_v. For reference, a straight line is plotted whose slope is 1 as predicted by (2.18). The first vertical line at $x_v - x_{\max} = 5\times10^{-2}$ is approximately where the density is no longer linear in the log–log plot. The percentile corresponding to the value $x_{\max} = x_v - 5\times10^{-2}$ is as high as 99.996. For example, the second vertical line corresponds to the 99.9th percentile. These lines are meant to indicate that the power-law behavior around the endpoint can begin very far into the tail of the density.

Fig. 4 demonstrates the effects that motivated this study: observation of a heavier tail of the peaks distribution of a response of a nonlinear dynamical system, while the presence of an unstable equilibrium (and possibility of capsizing) indicates a right finite upper bound and light tail. Analysis of peaks of the piecewise linear system with similar phase plane topology reproduces this effect. The tail actually has both properties — it is heavy for most of the distance to the unstable equilibrium, but it becomes light in the immediate vicinity of the end point. The reasons why this is occurring and how topology of the phase plane defines the tail structure is addressed in Section 3.

2.2.4. Transition to flat stiffness

Some aspects of dynamics of piecewise linear system with a flat portion of stiffness (i.e. trapezoid) was examined by Belenky et al. [30] following the discussion by Reed [31].

Consider the influence of a flat portion of the stiffness on the tail structure (the flat portion of stiffness is extended to infinity after the "knuckle" point). Assume no damping and excitation after the "knuckle" point. Take the density (2.23) and let k_1 approach 0, while keeping x_m fixed.

Note first that

$$x_v = x_m\frac{1 + k_1}{k_1} \quad \text{and} \quad x_v - x_m = \frac{x_m}{k_1}. \tag{2.24}$$

Moreover, $\lambda^2 = w_0^2 k_1$. Then, the density (2.23) becomes

$$\begin{aligned}
&\frac{\lambda^2(x_v - x)e^{\frac{\lambda^2}{2\sigma_{\dot{x}}^2}(x_v - x)^2}}{\sigma_{\dot{x}}^2(e^{\frac{\lambda^2}{2\sigma_{\dot{x}}^2}(x_v - x_m)^2} - 1)} = \frac{\lambda^2(x_v - x)e^{\frac{\lambda^2}{2\sigma_{\dot{x}}^2}[(x_v - x)^2 - (x_v - x_m)^2]}}{\sigma_{\dot{x}}^2(1 - e^{-\frac{\lambda^2}{2\sigma_{\dot{x}}^2}(x_v - x_m)^2})} \\
&= \frac{\lambda^2(x_v - x)e^{\frac{\lambda^2}{2\sigma_{\dot{x}}^2}[(x_v - x_m + x_m - x)^2 - (x_v - x_m)^2]}}{\sigma_{\dot{x}}^2(1 - e^{-\frac{\lambda^2}{2\sigma_{\dot{x}}^2}(x_v - x_m)^2})} \\
&= \frac{\lambda^2(x_v - x)e^{\frac{\lambda^2}{2\sigma_{\dot{x}}^2}[2(x_v - x_m)(x_m - x) + (x_m - x)^2]}}{\sigma_{\dot{x}}^2(1 - e^{-\frac{\lambda^2}{2\sigma_{\dot{x}}^2}(x_v - x_m)^2})} \\
&= \frac{w_0^2(x_m(1 + k_1) - xk_1)e^{\frac{w_0^2 x_m}{\sigma_{\dot{x}}^2}(x_m - x)}e^{\frac{w_0^2 k_1}{\sigma_{\dot{x}}^2}(x_m - x)^2}}{\sigma_{\dot{x}}^2(1 - e^{-\frac{w_0^2 x_m^2}{2\sigma_{\dot{x}}^2 k_1}})} \\
&\to \frac{w_0^2 x_m}{\sigma_{\dot{x}}^2}e^{-\frac{w_0^2 x_m}{\sigma_{\dot{x}}^2}(x - x_m)}, \quad x > x_m, \quad \text{as } k_1 \downarrow 0,
\end{aligned} \tag{2.25}$$

that is, the density converges to the exponential pdf with parameter $\frac{w_0^2 x_m}{\sigma_{\dot{x}}^2}$. This is illustrated in Fig. 5. The slope $-k_1$ of the decreasing part of the stiffness function is changed systematically from -1 to 0, as shown in the left plot of the figure. The right plot of the figure shows the corresponding changes in the distribution of the maximum. The heavy part of the tail becomes lighter, until it reaches the exponential

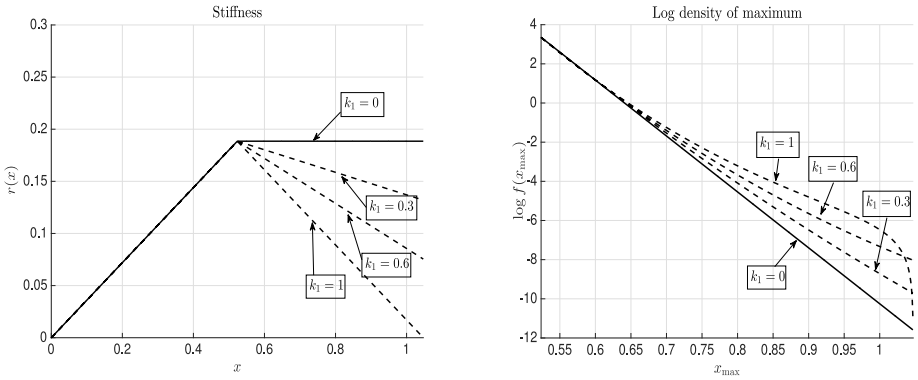

Fig. 5. Left: The stiffness function for varying choices of k_1. Right: The density $f(x_{\max})$ of the maximum value on the log vertical scale for varying choices of k_1.

distribution (2.25) for $k_1 = 0$. The "inflection point" moves to the right, until it eventually disappears when the position x_v of the unstable equilibrium goes to infinity.

The changes in the slope coefficient k_1 translate into the changes in the shape of stiffness. Thus, the shape of the stiffness function defines the shape of the tail after the "knuckle" point, while the position x_v of the unstable equilibrium defines the position of the "inflection point". The softening nonlinearity ($k_1 > 0$) thus seems to be responsible for the "two-tails" (heavy and light) structure of the tail. It disappears when k_1 becomes zero.

2.3. The distribution of the response

Section 2.2 concerned the distribution of the maximum value of the solution (2.1). Here, the focus is on the density of the response (2.1) itself, that is, the distribution of the excursion values of $x(t)$ above x_m over time $t_0 < t < t_1$, where $x(t_0) = x_m$. This density can be expressed as

$$f_{x(t)}(x) = C_1 \int_{G^{-1}(x)}^{\dot{x}_{\rm cr}} g(x, \dot{x}_1) f_{\dot{x}_1}(\dot{x}_1) d\dot{x}_1, \quad x_m < x < x_v, \tag{2.26}$$

where $\dot{x}_{\rm cr}$ is given by (2.4), $f_{\dot{x}_1}(\dot{x}_1)$ appears in (2.9), G^{-1} is the inverse of the function G in (2.11) and

$$g(x, \dot{x}_1)^{-1} = |x'(t)| \Big|_{t: x(t)=x}, \tag{2.27}$$

emphasizing the dependence on $\dot{x}_1$ in the notation $g(x, \dot{x}_1)$. The role of $g(x, \dot{x}_1)$ is illustrated in Fig. 6, left plot. The normalizing constant can be expressed as

$$C_1^{-1} = \frac{1}{2} \int_0^{\dot{x}_{\rm cr}} t_0(\dot{x}_1) f_{\dot{x}_1}(\dot{x}_1) d\dot{x}_1, \tag{2.28}$$

where $t_0 = t_0(\dot{x}_1) > 0$ satisfies $x(t_0) = x_m$ as above.

2.3.1. Special case of no damping

The density (2.26) can be evaluated more explicitly in the case of no damping. In this case, the function $G^{-1}(x)$ is given by (2.22). The function $g(x, \dot{x}_1)^{-1}$ can be expressed as

$$g(x, \dot{x}_1)^{-1} = H \sinh(\lambda t + \epsilon) \Big|_{t = \frac{1}{\lambda}(\cosh^{-1}(\frac{x_v - x}{-H}) - \epsilon)} = H \sinh\Big(\cosh^{-1}\Big(\frac{x_v - x}{-H}\Big)\Big)$$
$$= H\sqrt{\Big(\frac{x_v - x}{-H}\Big)^2 - 1} = \sqrt{\dot{x}_1^2 - \lambda^2((x_v - x_m)^2 - (x_v - x)^2)}$$
$$= \lambda^{-1}\sqrt{\dot{x}_1^2 - G^{-1}(x)^2},$$

since $-H = 2(AB)^{1/2} = \sqrt{(x_v - x_m)^2 - \dot{x}_1^2/\lambda^2}$. Then, letting $G^{-1}(x) = a$, the density (2.26) becomes, after a series of changes of variables,

$$f_{x(t)}(x) = C \int_a^{\dot{x}_{\rm cr}} \frac{z e^{-\frac{z^2}{2\sigma_{\dot{x}}^2}}}{\sqrt{z^2 - a^2}} dz = C' \int_{a^2}^{\dot{x}_{\rm cr}^2} \frac{e^{-\frac{w}{2\sigma_{\dot{x}}^2}}}{\sqrt{w - a^2}} dw$$
$$= C' e^{-\frac{a^2}{2\sigma_{\dot{x}}^2}} \int_0^{\dot{x}_{\rm cr}^2 - a^2} \frac{e^{-\frac{u}{2\sigma_{\dot{x}}^2}}}{\sqrt{u}} du = C'' e^{-\frac{a^2}{2\sigma_{\dot{x}}^2}} \int_0^{\sqrt{\dot{x}_{\rm cr}^2 - a^2}} e^{-\frac{v^2}{2\sigma_{\dot{x}}^2}} dv.$$

By recalling that $a^2 = G^{-1}(x)^2 = \lambda^2((x_v - x_m)^2 - (x_v - x)^2)$ and using the fact that $\dot{x}_{\rm cr}^2 - a^2 = \lambda^2(x_v - x)^2$, the density can be expressed as

$$f_{x(t)}(x) = C_0 \mathrm{erf}\Big(\frac{\lambda(x_v - x)}{\sqrt{2}\sigma_{\dot{x}}}\Big) e^{\frac{\lambda^2}{2\sigma_{\dot{x}}^2}(x_v - x)^2}, \quad x_m < x < x_v, \tag{2.29}$$

where $\mathrm{erf}(u) = \frac{2}{\sqrt{\pi}} \int_0^u e^{-z^2} dz$ is the error function and C_0 is a normalizing constant.

The difference between the densities of the response and the maximum in (2.29) and (2.23), respectively, is only in the terms $\mathrm{erf}(\lambda(x_v - x)/\sqrt{2}\sigma_{\dot{x}})$ in (2.29) and $x_v - x$ in (2.23). Note, in particular, that these two terms have the same asymptotic behavior up to a constant as $x \uparrow x_v$ or $x_v - x \downarrow 0$, since $\mathrm{erf}(u)$ behaves as $2u/\sqrt{\pi}$ for small u. The two densities are depicted in Fig. 6, right plot, for the same parameter values as in Fig. 4.

2.4. Power-law tail

Further insight can be gained from Fig. 7 where the densities of the response and the maximum are depicted in the log–log plot. The densities now appear almost linear, especially that of the maximum density, over a wide range of values. This suggests a power-law behavior of the densities, that is, the behavior $f(x) \approx Cx^{-\alpha-1}$ over a range of values x, with $\alpha > 0$.

On the other hand, the power-law behavior is not apparent from the analytic expressions of the densities of the response and the maximum in (2.23) and (2.29). This can nevertheless be explained through the following argument. Consider the case of the density of the maximum in (2.23). This density should appear linear at least around the value $x = x_m$ in the log–log plot (which it does according to Fig. 7), supposing that a certain condition holds.

Indeed, by considering the log of the density (2.23) around $x = x_m$ and keeping track of the first and second order terms only in the approximations below, observe that

$$\begin{aligned}
\log f_{x_{\max}}(x) &= c_1 + \log(x_v - x) + \frac{\lambda^2}{2\sigma_{\dot{x}}^2}(x_v - x)^2 \\
&= c_2 + \log\Big(1 - \frac{x - x_m}{x_v - x_m}\Big) + \frac{\lambda^2}{2\sigma_{\dot{x}}^2}(x_v - x_m)^2\Big(1 - \frac{x - x_m}{x_v - x_m}\Big)^2 \\
&\approx c_3 - \frac{x - x_m}{x_v - x_m} - \frac{1}{2}\Big(\frac{x - x_m}{x_v - x_m}\Big)^2 - \frac{\lambda^2}{\sigma_{\dot{x}}^2}(x_v - x_m)(x - x_m) \\
&\quad + \frac{\lambda^2}{2\sigma_{\dot{x}}^2}(x - x_m)^2 \\
&= c_3 - \Big(\frac{1}{x_v - x_m} + \frac{\lambda^2}{\sigma_{\dot{x}}^2}(x_v - x_m)\Big)x_m\Big(\frac{x}{x_m} - 1\Big) \\
&\quad + \Big(\frac{\lambda^2}{2\sigma_{\dot{x}}^2} - \frac{1}{2(x_v - x_m)^2}\Big)x_m^2\Big(\frac{x}{x_m} - 1\Big)^2 \\
&\approx c_3 - (\alpha + 1)\log\frac{x}{x_m},
\end{aligned} \tag{2.30}$$

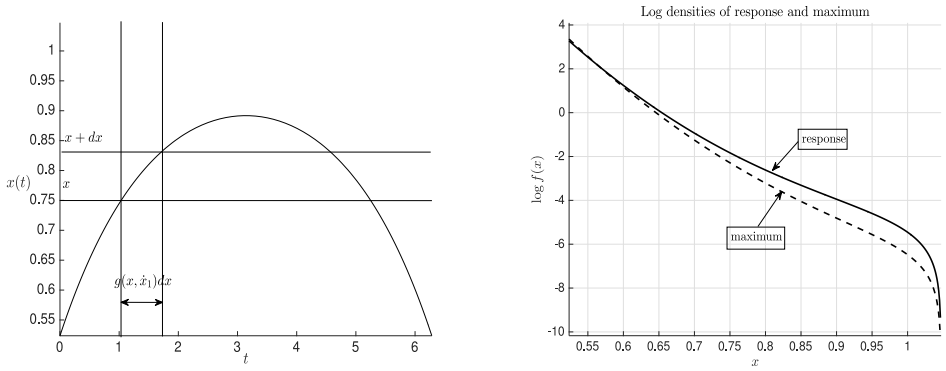

Fig. 6. Left: Illustration of the role of $g(x, \dot{x}_1)$. Right: The densities $f_{x(t)}$ and $f_{x_{\max}}$ of the response and the maximum value on the log vertical scale.

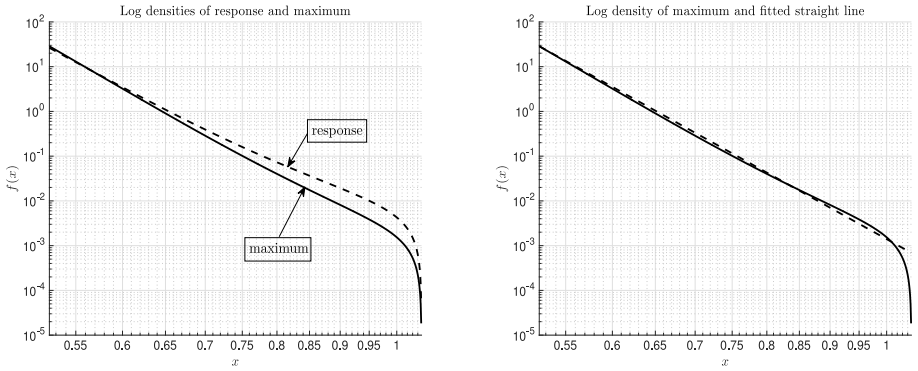

Fig. 7. The densities $f_{x(t)}$ and $f_{x_{\max}}$ of the response and the maximum value in the log–log plot.

provided for the last approximation that

$$\alpha + 1 \approx \Big(\frac{1}{x_v - x_m} + \frac{\lambda^2}{\sigma_{\dot{x}}^2}(x_v - x_m)\Big)x_m \approx 2\Big(\frac{\lambda^2}{2\sigma_{\dot{x}}^2} - \frac{1}{2(x_v - x_m)^2}\Big)x_m^2. \quad (2.31)$$

The exponent $\alpha + 1$ then defines the slope of the line in the log–log plot of the density around $x = x_m$. The power-law behavior is analyzed further in Section 4.2.

3. White noise excitation and interpretation of the tail structure

In this section, the system (1.1) is considered again but now subjected to white noise excitation, $y(t) = s\dot{W}(t)$, where W is a standard Brownian motion and s is the intensity of the white noise excitation. Despite the broadband character of the stochastic forcing, which is not realistic for the description of wave excitation, its mathematical structure allows for the derivation of closed-form expressions for the non-Gaussian pdf of the response. One of the objectives of this work is to understand whether the derived results, based on white noise excitation, can be related to the corresponding results when the excitation is correlated. Such a conjecture follows from the observation that in ship motion, inertia plays a dominant role, and therefore high frequency content in the excitation is "filtered out" naturally by the system. That would immediately imply that the primary factor defining the properties of the pdf tail is not the correlation structure of the excitation, but rather the intrinsic dynamics of the system (in this case the restoring force). Such a conclusion will help interpreting the non-Gaussian properties of the tail (for both white and colored noises) and directly relating its form with the phase portrait of the unforced and undamped dynamical system.

For single-degree-of-freedom systems like (1.1), the full (unconditional) pdf can be found for the statistical steady state by direct solution of the associated Fokker–Planck–Kolmogorov (FPK) equation. More specifically, the pdf in the statistical steady state is given by

$$f_\infty(x, \dot{x}) = Ce^{-\frac{4\delta}{s^2}\mathbb{H}(x,\dot{x})}, \quad (3.1)$$

where

$$\mathbb{H}(x, \dot{x}) = \frac{1}{2}\dot{x}^2 + V(x)$$

is the Hamiltonian of the system, and C is a normalizing constant (e.g. [32], Theorem 1.6, p. 34 or p. 334). Based on the unconditional pdf (3.1), the constrained pdf for the response x can now be expressed inside the separatrix, that is, within the two heteroclinical orbits that enclose the stable center and connect the two unstable equilibria in the phase space as in Fig. 1. Denote the locus of the separatrix points by $(x_s, \dot{x}_s)$. This separatrix is defined implicitly through the Hamiltonian function if the unstable equilibria $\pm x_v$ is known:

$$\mathbb{H}(x_s, \dot{x}_s) = \mathbb{H}(\pm x_v, 0) \equiv \mathbb{H}^*. \quad (3.2)$$

The last equation can be solved explicitly for $\dot{x}_s$:

$$\dot{x}_s(x) = \pm\sqrt{2\,(\mathbb{H}^* - V(x))}. \quad (3.3)$$

In this way, the *conditional pdf* within the separatrix is obtained as

$$f_s(x) = C\int_{-\dot{x}_s(x)}^{+\dot{x}_s(x)} f_\infty(x, \dot{x})\,d\dot{x}, \quad -x_v < x < x_v, \quad (3.4)$$

where C is another normalizing constant. Although the analysis is valid for a general potential function $V(x)$, for the sake of presentation, the focus is on the special case of the piecewise linear system considered in Section 2.

In Fig. 8 (upper left plot), the potential of the system is presented and compared to the corresponding linear system (i.e. the one characterized by a linear restoring function $r(x) = \omega_0^2 x$). In the same figure, the pdf of the response (under the condition of non-capsizing, i.e. non-crossing of the separatrix) is also presented and compared to the Gaussian pdf that corresponds to the same system but with linear restoring function. As can be observed, the tail of the constrained nonlinear oscillator consists of three different regimes:

(i) a Gaussian core,

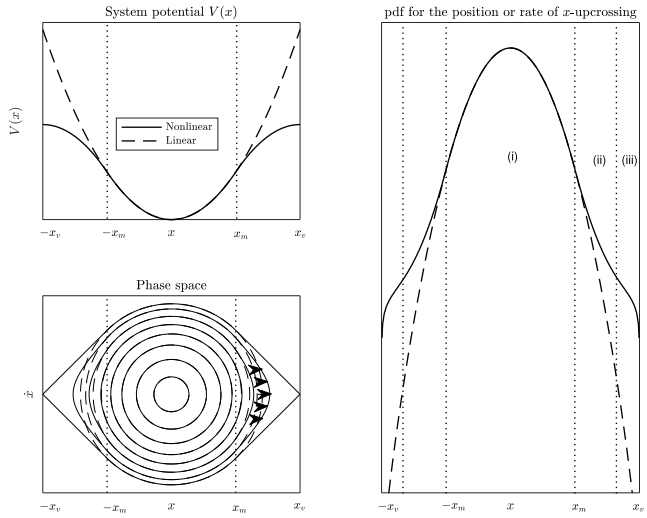

Fig. 8. Upper left: Potential function for the piecewise linear system (solid curve) and the corresponding linear system (dashed curve); Lower left: Phase portrait for the piecewise linear system and the linear system; Right: Probability density function $f_s(x)$ for both systems considered with the three regions (i), (ii) and (iii). Dotted lines indicate $\pm x_m$ throughout.

(ii) a heavy-tail region, and
(iii) a light-tail region.

A detailed interpretation of this pdf form in connection with the dynamical properties of the system is provided below.

3.1. Gaussian core and heavy-tail regime

The phase portraits for the two systems are shown in the lower left plot of Fig. 8. For $|x| < x_m$ the two systems are identical resulting in (at the statistical level) the presence of a Gaussian "core" for the nonlinear system, which dominates the response statistics close to the stable equilibrium.

When moving to higher energies, trajectories begin to depart from the linear regime and enter the nonlinear regime, with a deformation of the linear-system phase portrait due to the presence of softening nonlinearity. The softening nonlinearity results in stretching of the trajectories to higher values of x compared with the trajectories of the linear system with equal energy. At the same time, the probability of occurrence of each of those nonlinear trajectories is governed by the Gaussian "core", which is fairly identical for the two systems, i.e. trajectories having the same energy have equal probability of occurrence in the two systems. From these two observations, the phase space stretching of the nonlinear system will be reflected in the response pdf through increase of the probability for higher values of x.

Indeed, as observed in the right plot of Fig. 8 where the pdfs of the two systems are shown, when moving away from the Gaussian "core", i.e. for values $|x| > x_m$ the pdf exhibits a heavy tail structure. This heavy tail is a direct manifestation of the deformation (stretching) of the phase space (due to the presence of nonlinearity) which has the following characteristics: it is zero or negligible for small values of $|x|$ so that the Gaussian core of the statistics is not influenced, and it is more pronounced for larger values of $|x|$ leading to larger responses of high energy trajectories compared to the linear system. In this sense, the nonlinearity of the system acts so that it does not change the probability of occurrence of each trajectory (or of each energy level) but only their shape, giving higher probability to larger responses.

3.2. Light-tail regime

As discussed in Section 3.1, suitable nonlinearity can lead to the formation of heavy tails. However, the heavy tail must turn light at a certain point as more and more trajectories lead to the second stable equilibrium. Thus, for the conditional response pdf, a saturation point exists where the heavy-tail behavior ceases to exist and light tails emerge eventually. This is the transition from the region (ii) to (iii) in the right plot of Fig. 8. To understand this transition better, the conditional pdf is expressed in terms of the system characteristics. By the relations (3.1) and (3.4),

$$f_s(x) = C_x e^{-\frac{4\delta}{s^2}V(x)} \int_{-\dot{x}_s(x)}^{+\dot{x}_s(x)} C_{\dot{x}} e^{-\frac{\dot{x}^2}{2\sigma_{\dot{x}}^2}} d\dot{x}, \tag{3.5}$$

where

$$\sigma_{\dot{x}}^2 = \frac{s^2}{4\delta} \tag{3.6}$$

and $C_x, C_{\dot{x}}$ are the normalizing constants for the two corresponding marginals.

The first term in the above product expresses the contribution of the nonlinear restoring force and contains information about the deformation of the phase space. It is the term that results in the heavy tail character of the distribution away from the Gaussian "core". The second term is related exclusively to the conditioning that is imposed so that the system response does not cross the separatrix. For system energy where $\sigma_{\dot{x}}$ is small, compared with the vertical separatrix radius, the integral term is approximately equal to 1. This is because the integral extends over the full effective support of the Gaussian distribution for the velocity.

However, when moving closer to the unstable equilibria $\pm x_v$, i.e. the value of x becomes large, the integral term deviates from 1 since the local width of the separatrix becomes comparable with or even smaller than the effective support of the velocity marginal. The integral term becomes much smaller, thereby reducing significantly the pdf value. This is the underlying reason for the eventual formation of light tails when approaching the unstable equilibria.

3.2.1. Estimation of the light-tail domain

To quantify a distance from x_v where the influence of the second term in (3.5) becomes important, the local width of the separatrix $\dot{x}_s(x)$ around x_v is compared to the effective support of the $\dot{x}$ marginal, measured through the standard deviation $\sigma_{\dot{x}}$. First, approximate $\dot{x}_s(x)$ around x_v by a Taylor expansion:

$$\dot{x}_s(x) = \dot{x}_s(x^*) + \frac{\partial \dot{x}_s}{\partial x}(x_v)(x - x_v) + O\left((x - x_v)^2\right). \tag{3.7}$$

Clearly, $\dot{x}_s(x_v) = 0$ and now the slope of the separatrix close to the unstable equilibrium has to be estimated. From the relation (3.2) that defines the separatrix,

$$\frac{\partial \mathbb{H}}{\partial x} dx + \frac{\partial \mathbb{H}}{\partial \dot{x}} d\dot{x} = 0,$$

which implies that

$$\frac{\partial \dot{x}_s}{\partial x} = -\lim_{x \uparrow x_v} \frac{\frac{\partial \mathbb{H}}{\partial x}}{\frac{\partial \mathbb{H}}{\partial \dot{x}}}.$$

Substitution of the Hamiltonian and application of L'Hospital's rule yield

$$\frac{\partial \dot{x}_s}{\partial x} = -\lim_{x \uparrow x_v} \frac{\frac{\partial V}{\partial x}}{\dot{x}_s} = -\frac{\frac{\partial^2 V}{\partial^2 x}}{\frac{\partial \dot{x}_s}{\partial x}}.$$

Therefore,

$$\left(\frac{\partial \dot{x}_s(x_v)}{\partial x}\right)^2 = -\frac{\partial^2 V(x_v)}{\partial^2 x}. \tag{3.8}$$

By the expression (3.8), the separatrix in the vicinity of the unstable equilibrium can be approximated as follows. The integral term in the conditional pdf becomes important when the width of the separatrix is comparable (i.e. sufficiently small) with the standard deviation for the velocity $\sigma_{\dot{x}}$. In particular,

$$\dot{x}_s(x) \sim \sigma_{\dot{x}}. \tag{3.9}$$

By the Taylor expansion (3.7) for the separatrix and the relation (3.8), the condition (3.9) takes the form

$$\sqrt{-\frac{\partial^2 V(x_v)}{\partial^2 x}}\Delta x \sim \sigma_{\dot{x}}, \tag{3.10}$$

where $\Delta x = x - x^*$ is the size of the layer over which the light tail is formed. This yields

$$\Delta x \sim \frac{\sigma_{\dot{x}}}{\sqrt{-\frac{\partial^2 V(x_v)}{\partial^2 x}}}. \tag{3.11}$$

The derivation of (3.11) relies on the smoothness of the separatrix as well as the Gaussian distribution of the velocity marginal. To this end, the analysis is valid also for systems of the same form where the excitation is a correlated stochastic process (see Section 3.2.2 below). For the special case of white noise considered here, $\sigma_{\dot{x}}$ is given by (3.6) and hence (3.11) becomes

$$\Delta x \sim \frac{s}{\sqrt{-4\delta\frac{\partial^2 V(x_v)}{\partial^2 x}}}. \tag{3.12}$$

3.2.2. Connection to piecewise linear system with correlated excitation

As indicated above, the derivation leading to (3.11) is expected to work for nonlinear systems driven by correlated excitations. Indeed, this is illustrated here on the piecewise linear system (1.1)–(1.3) considered in Section 2. For the potential function $V(x)$ of the piecewise linear system given in (1.3), the width of the light-tail regime (3.11) is given by

$$\Delta x \sim \frac{\sigma_{\dot{x}}}{\sqrt{k_1\omega_0^2}}. \tag{3.13}$$

For the case of no damping and no excitation above the "knuckle" point, this can be expressed as

$$\Delta x \sim \frac{\sigma_{\dot{x}}}{\lambda} \tag{3.14}$$

On the other hand, consider the pdf of the maximum value given by (2.23). The logarithm of the pdf (2.23) has an inflection point given by

$$x_{\text{infl}} = x_v - \frac{\sigma_{\dot{x}}}{\lambda}. \tag{3.15}$$

Thus, even from the perspective of (2.23) and the location of the inflection point, the light tail width can be thought as $\frac{\sigma_{\dot{x}}}{\lambda}$, which is exactly the same as the right-hand side of (3.14). In the next section, the role of the light-tail region on the POT approach in extreme value analysis is examined.

4. Extreme value analysis using generalized Pareto distribution

As the distributions of response and maxima of the piecewise linear oscillator (1.1)–(1.3) are known, a question of interest here is how standard extreme value analysis based on the POT and the GPD (1.4) performs on the data generated by (1.1)–(1.3). Comparing features of the known distribution tail to the results of the POT analysis [19,20] should lead to a better understanding about the performance of the approach applied to ship motions, as well as to other oscillator-like systems.

The POT approach and the GPD fits are studied below for the random oscillator (1.1)–(1.3) from several angles. In Section 4.1, the behavior of the estimates of the shape parameter as a function of threshold for a range of values of the oscillator model is examined. In Section 4.2, the power-law behavior of the distribution tail of the oscillator noted in Section 2.4 is revisited. In Section 4.3, the question is when the point of vanishing stability x_v can be estimated through the POT approach, which relates the findings to the light-tail region of the oscillator discussed in Sections 2 and 3.

4.1. Shape parameter estimates

The definition (1.4) of the GPD and the discussion following it point to the special role played by the shape parameter ξ. In particular, the cases of positive and negative shape parameters are quite different. A negative shape parameter $\xi < 0$ corresponds to the GPD having a finite endpoint at $x = \mu + \sigma/(-\xi)$. The distribution of the maximum or the response of the oscillator (1.1)–(1.3) derived in Section 2 naturally has such an endpoint at the point of vanishing stability x_v. Moreover, $\xi > 0$ is associated with the power-law behavior of the GPD pdf with the exponent $-1/\xi - 1$ around the endpoint. In view of (2.18), for the oscillator (1.1)–(1.3),

$$-\frac{1}{\xi} - 1 = -\frac{\lambda_1 - \lambda_2}{\lambda_2} - 1,$$

that is,

$$\xi = \frac{\lambda_2}{\lambda_1 - \lambda_2} \in (-1, 0). \tag{4.1}$$

In the case of no damping above the "knuckle" point,

$$\xi = -\frac{1}{2}. \tag{4.2}$$

Despite the distribution of the maximum or the response of the oscillator (1.1)–(1.3) always having an endpoint at x_v, a negative shape parameter $\xi < 0$ will not necessarily be estimated from data. As already observed in Section 2.4, a power-law tail is expected in some cases. The power-law tail with the exponent α as in Section 2.4 is associated with the positive shape parameter value $\xi = 1/\alpha > 0$ of the GPD. From another perspective, as discussed in Section 2.2.2, the region of the power-law behavior around the endpoint can occur too far into the tail from a practical standpoint.

For simplicity, focusing on the pdf (2.23) of the oscillator maximum response in the case of no damping above the "knuckle" point, characterized by the shape parameter ξ in (4.2), the pdf can be examined through the lens of the GPD as follows. In Fig. 9, the plots of the average estimated shape parameter values are presented as functions of threshold, as explained in greater detail below. (The estimates are obtained through the maximum likelihood estimation as in [5,20].) A varying threshold is considered since in practice it is selected through a data driven method.

The underlying oscillator parameters are the same as those used at the end of Section 2.1 except that a range of the parameters $\sigma_{\dot{x}}$ and k_1 is considered: the first plot of Fig. 9 corresponds to $\sigma_{\dot{x}} = 0.03$ rad/s, the second plot to $\sigma_{\dot{x}} = 0.08$ rad/s, and the third plot to $\sigma_{\dot{x}} = 0.13$ rad/s. In each of these plots, three different values of k_1 are considered: $k_1 = 0.5$, 1 and 2. Thresholds μ are taken above the "knuckle" point $x_m = \pi/6 = 0.5236$ rad but below $0.95x_v$, where $x_v = x_m(1 + k_1)/k_1$ is the point of vanishing stability in (2.24). For each set of the fixed parameters of the oscillator model and a threshold, 100 datasets of length 400 are generated above the threshold according to the pdf (2.23) and the average value of the shape parameter estimates over these 100 datasets are plotted. The vertical lines in the plots correspond to the points of vanishing stability x_v (dashed lines) and the inflection points x_{infl} (dotted lines) calculated according to (3.15).

The average value of the shape parameter estimates grows and then falls sharply with the increase of the threshold for $\sigma_{\dot{x}} = 0.03$ rad/s; this tendency is observed for all three values of the slope k_1 when $\sigma_{\dot{x}} = 0.03$ rad/s. The effect of the stretching phase plane in Fig. 8 is stronger with larger amplitude of the response. Increasing the threshold excludes small peaks and leaves large ones. Thus, the increased influence of

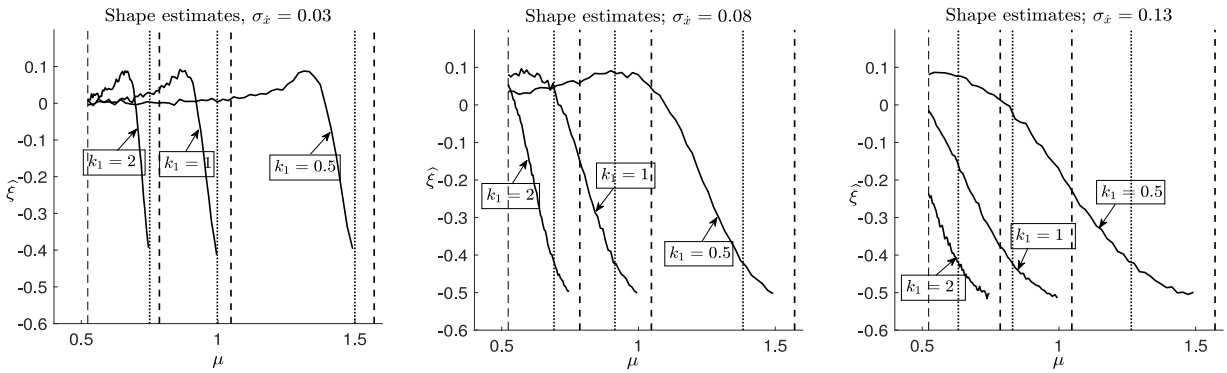

Fig. 9. Average shape parameter estimates as functions of threshold, for $\sigma_{\dot{x}} = 0.03$ rad/s, 0.08 rad/s, 0.13 rad/s and $k_1 = 0.5$, 1, 2.

the effect of phase plane stretching leads to an increase in the shape parameter estimate until the population of larger peaks starts to drop because of a transition to another stable equilibrium ("capsizing").

Continuing consideration of the case with $\sigma_{\dot{x}} = 0.03$ rad/s, the decrease of the slope coefficient k_1 does not change the shape of the curve, but stretches and shifts it to the right. This is expected as the position of the unstable equilibrium x_v moves to the right with the decrease of the slope coefficient k_1; see Fig. 5. In the limit of $k_1 = 0$, the distribution of peaks becomes exponential (see (2.25)), from which zero values of the shape parameter estimates are expected for all the thresholds. On the other hand, Fig. 5 shows a heavier tail when k_1 increases; this makes the shape parameter estimates grow faster for smaller thresholds, which is also seen in the left plot of Fig. 9.

Consider now the effect of increasing $\sigma_{\dot{x}}$ from 0.03 to 0.08 rad/s on the curve corresponding to $k_1 = 0.5$, shown in the first two plots of Fig. 9. Increase of the standard deviation of the velocities corresponds to the increase of the excitation, and hence to larger velocities at the crossing of the "knuckle" point. Naturally, this leads to the growth of the population of larger peaks and is reflected in the faster increase of the shape parameter estimates. Indeed, with the increase of excitation, capsizing is more probable, so its influence is "felt" for smaller thresholds. Regarding the effect of increasing k_1, similarly to above, the curve is shrunk and shifted to the left; however, shrinkage seems to be prevalent. Finally, the case $\sigma_{\dot{x}} = 0.13$ rad/s (the last plot in Fig. 9) can be seen as a part of this tendency, only the increase has been "shadowed" by the "knuckle" point. The behavior of the curves corresponding to $k_1 = 1$ and $k_1 = 2$ does not contradict this description.

The inflection point (represented by dotted lines for the various cases) seems to be overestimated by (3.15), as negative parameters are estimated for lower thresholds. This means that the "capsizing" influence starts to affect the distribution before the vertical distance to the separatrix decreases to $\sigma_{\dot{x}}$ (see Section 3.2.1). The inflection point was searched from the condition of comparability, i.e. with the accuracy of up to a constant. The numerical relationship of the position of the inflection point and $\sigma_{\dot{x}}$ still needs to be studied. For a threshold in the light-tail region of the distribution (that is, larger than the inflection point), the shape parameter estimates are quite close to the value −0.5, which is expected according to (4.2) as discussed above.

In general, the plots of Fig. 9 illustrate the fact that depending on the underlying oscillator parameters and the likelihood of the transition to another stable equilibrium, the structure of the pdf (2.23) is quite different.

4.2. Power-law tail behavior revisited

Recall from Section 2.4 that the distribution of the maximum or the response of the oscillator (1.1)–(1.3) can appear to have a power-law tail. In the POT framework, a power-law tail corresponds to the GPD with a positive shape parameter $\xi > 0$, with a larger $\xi > 0$ corresponding to a heavier power-law tail. In particular, Fig. 9 in

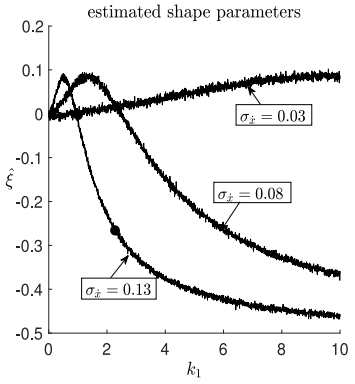

Fig. 10. Estimated shape parameters from samples of 400 data points from the GPD fitted to $f_{x_{\max}}$ in (2.23), for $\sigma_{\dot{x}} = 0.03$ rad/s, 0.08 rad/s and 0.13 rad/s. Circles correspond to the values of k_1 satisfying the equality of the right two expressions in (2.31).

Section 4.1 shows that depending on the choice of a threshold and the underlying oscillator parameters, a positive shape parameter can be estimated. Several basic questions related to the power-law tail behavior are of interest here. How large $\xi > 0$ can be observed with the oscillator (1.1)–(1.3)? What system parameter values are associated with the largest $\xi > 0$?

To answer these questions, random samples are generated from the pdf (2.23) of the maximum value of the oscillator in the case of no damping above the "knuckle" point over a range of parameter values $\sigma_{\dot{x}} = 0.03$ rad/s, 0.08 rad/s and 0.13 rad/s, and $0 \le k_1 \le 10$ with step-size 0.005. (The rest of the oscillator parameters are the same as at the end of Section 2.1.)

Both positive and negative shape parameters can be estimated for many different values of $\sigma_{\dot{x}}$ and k_1 in Fig. 10. The largest values of $\hat{\xi}$ in the figure are around 0.1. From the GPD perspective, a distribution tail with $\xi = 0.1$ is not very "heavy": such distribution has all its moments finite up to order 10.

Examination of the figure in view of the discussion in Section 2.4 is also interesting. The equality of the right two expressions of (2.31) yields a relationship between k_1 and $\sigma_{\dot{x}}$, with the corresponding value of α in (2.31) and hence $1/\alpha = \xi$. For the three choices of $\sigma_{\dot{x}}$ in Fig. 10, the corresponding values of k_1 (making the right two expressions of (2.31) equal) are depicted by circles in the figure. Note that the estimated values of $\hat{\xi}$ at the circles are not necessarily positive (nor necessarily the largest values of $\hat{\xi}$ observed for a fixed value of $\sigma_{\dot{x}}$). That is, the analysis carried out in Section 2.4 is not sufficient to observe a power-law behavior (estimate a positive shape parameter). As argued in the next section, observing a power-law behavior also depends on the scope of the light-tail region. Finally, Fig. 10 is consistent with Fig. 9. For example, for $k_1 = 2$, the estimate of ξ in Fig. 9 with the "knuckle" point as the threshold is negative for $\sigma_{\dot{x}} = 0.13$ rad/s.

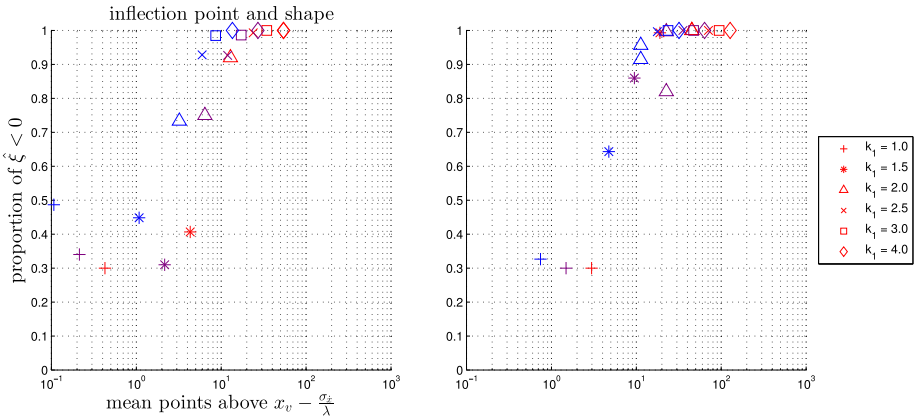

Fig. 11. Proportion of negatively estimated shape parameters in 150 to 300 records of the oscillator data. Left: $H_s = 9$ m; right: $H_s = 10$ m. Blue: 50 h; purple: 100 h; red: 200 h . (For interpretation of the references to color in this figure legend, the reader is referred to the web version of this article.)

4.3. Estimating the point of vanishing stability

As discussed in Section 4.1, the distribution of the maximum or the response of the oscillator (1.1)–(1.3) derived in Section 2 is associated with the GPD having a negative shape parameter $\xi < 0$ in (4.1) (and $\xi = -0.5$ in (4.2) in the case of no damping above the "knuckle" point). Moreover, Fig. 9 of that section shows clearly that a negative shape parameter is not necessarily estimated in practice. The basic question is then: when will a negative shape parameter be in fact estimated from data? As Fig. 9 already suggests, this might be related to the light-tail region, which is the region above the inflection point (3.15) discussed in Sections 2 and 3.

To address these issues, the frequency of the estimation of the negative shape parameters is examined on the data simulated from the oscillator (1.1)–(1.3). For each of the values of the significant wave height $H_s = 6$ m, 9 m and 10 m, and the slope $k_1 = 0.5, 1, 1.5, 2, 2.5, 3$ and 4, 30,000 h of the data from the oscillator (1.1)–(1.3) are generated. The values of $H_s = 6$ m, 9 m and 10 m correspond to $\sigma_{\dot{x}} = 0.0632$ rad/s, 0.0948 rad/s and 0.105 rad/s, respectively, which are comparable to the values of $\sigma_{\dot{x}}$ considered in Figs. 9 and 10 for the pdf (2.23). (Unlike in Sections 4.1 and 4.2, the data here were actually generated from the oscillator.) The data were then split into shorter records; either 600 records of 50 h each, 300 records of 100 h each, or 150 records of 200 h each. Within each record, the POT approach was applied to estimate the shape parameter ξ. Threshold values were selected automatically as in [5,20], and the maximum likelihood estimate for the shape parameter $\hat{\xi}$ was calculated, as well as the length of the data above the inflection point (3.15). In the latter expression, the theoretical values of $\sigma_{\dot{x}}$ listed above were employed (see Section 2.1).

Fig. 11 summarizes the results by comparing the mean number (across all records of a given set of oscillator parameters) of points above the inflection point to the proportion of records which estimated a negative shape parameter. Notably, enough information in the record to correctly estimate a negative shape parameter is contained at around 10 data points above the inflection point. For records with very few points above the inflection point, shape parameters are estimated positively and negatively with close to equal proportion, which is consistent with an exponential fit (i.e. with $\xi = 0$). This was the case when $H_s = 6$ m (not shown) and for the lower slopes when $H_s = 9$ m or 10 m. In conclusion, a primary indicator of the ability to estimate a negative shape parameter and, in turn, a finite endpoint of the maximum of the oscillator is the presence of data above the inflection point (that is, in the light-tail region). In particular, parameters which give a pdf that has a shorter region from x_m to the inflection point relative to the region from the inflection point to x_v contribute to estimating a negative shape parameter, due to the greater probability above the inflection point.

5. Summary and conclusions

To understand the structure of the tail of a nonlinear dynamical system, the oscillator (1.1)–(1.3) with a piecewise linear restoring force was considered. This oscillator is known to model most principal properties of a dynamical system with softening nonlinearity [2].

The response of (1.1)–(1.3) below or above the "knuckle" point was expressed in closed form. This allows solving for the response pdf (2.26) above the "knuckle" point if the excitation above the "knuckle" point is neglected. The influence of the excitation above the "knuckle" point is small anyway, as the resonance is not possible there [21]. If damping above the "knuckle" point is also neglected, the response pdf can be expressed in closed form; see (2.29).

Analogously, a closed form solution was derived for the maxima of the response for the no-damping case; see (2.23). If the damping is present, the maxima pdf can be expressed by (2.12). However, a closed form solution is still available in the vicinity of the unstable equilibrium, described by the relation (2.18).

The other simplification used in this study is neglecting correlation in the excitation, by modeling it as white noise and thus assuming that the response distribution tail structure is mostly the result of nonlinearity of the oscillator rather than internal dependence on the excitation. The pdf of the response becomes available as a solution of the associated FPK equation; see (3.1).

Analysis of the pdf of the response and its maxima above the "knuckle" point using both approaches has shown that the tail first becomes heavy because of stretching of the phase plane and then becomes light because more and more trajectories lead to capsizing. The following arguments are presented to support this conclusion:

(i) The computed pdf of the response maxima is above the pdf of the corresponding linear system. It is described by a heavy-tail (possibly power-law) region and then a collapse towards the unstable equilibrium (a light-tail region) – see Section 2.2 and Fig. 4, in particular.

(ii) Similar findings apply to the pdf of the response — see Section 2.3 and Fig. 6, in particular.

(iii) Changing the shape of stiffness changes the tail: decrease of the slope after the "knuckle" point makes the tail lighter, with a limit of exponential tail for a flat restoring term — see Section 2.2.4 and Fig. 5, in particular.

(iv) The distribution of a white noise-excited system shows a heavy tail above the "knuckle" point due to the phase plane stretching — see Section 3.1 and Fig. 8, in particular.

(v) The probability of a non-capsizing trajectory is dramatically decreased when approaching the unstable equilibrium, where the distance to the separatrix becomes comparable with the conditional standard deviation of the derivative of the response;

the latter condition is used to estimate a position of the "inflection" point, where the tail switches from heavy to light — see Section 3.2.

(vi) Monte Carlo simulated samples were used to fit the GPD parameters; the combination of positive and negative values of the shape parameter estimates were found where heavy and light tails were expected — see Section 4, Figs. 9 and 10, in particular.

In other words, softening nonlinearity leads to a heavy and light tail combination for the non-capsizing response and its maxima.

What are implications and practical importance of this conclusion?

(i) The question posed at the end of Section 1 was answered: observing heavy tails when light tail may be expected while extrapolating roll peak data is natural and related to the fact that ship rolling is described by softening nonlinear system (as a ship usually has a limited range of stability).

(ii) Statistical uncertainty associated with extrapolation of practical volume of ship motion samples is rather large (e.g. [33]). As shown by Glotzer et al. [20], introducing a physical information by relating the GPD parameters allows a significant decrease of the confidence intervals. To do this, the structure of the distribution tail should be known.

Where can this work be taken from here?

(i) More study is needed on the inflection point; while the principle is clear, the accuracy of the prediction needs to be improved.

(ii) Glotzer et al. [20] have related shape and scale parameters for the case of the light tail by postulating the upper bound of the distribution. How can this be done for the heavy tail where an upper bound does not exist?

Another principal issue is related to the modeling of excitation. The spectral-based model (see Appendix for details), while conventional in Naval Architecture [34,35], is known to work up to the second moments. The adequacy of this model is not clear for the extreme value problems. One of the alternatives is the autoregressive model (ARM) that has seen wide application in other engineering fields, and while it was considered for modeling waves in the 1980s [36], the interest was renewed recently [37,38]. Degtyarev and Reed [39] have shown that ARM reproduces nonlinear properties embedded in its auto-covariance function, so it may work well for extreme events.

Acknowledgments

The work described in this paper has been funded by the Office of Naval Research (ONR), United States under Dr. Thomas Fu and Dr. Woei-Min Lin and by the Naval Surface Warfare Center Carderock Division (NSWCCD) Independent Applied Research (IAR) program. Participation of Prof. Pipiras and Prof. Sapsis was facilitated by the Summer Faculty Program supported by ONR, United States and managed by NSWCCD under Dr. Jack Price, who also manages IAR program. Part of funding for Prof. Pipiras and Prof. Sapsis was provided by ONR grants N00014-19-1-2029 under Dr. Woei-Min Lin and N00014-15-1-2381 under Dr Reza Malek-Madani, respectively. Participation of Mr. Glozter was facilitated by the NSWCCD Naval Research Enterprise Internship Program (NREIP) program, managed by Ms. Rachel Luu.

Discussions with Dr. Art Reed, Ken Weems, Tim Smith, Brad Campbell of NSWCCD and Prof. Kostas Spyrou of National Technical University of Athens (Greece) were very fruitful.

Appendix. Spectral density of correlated excitation

The parameters in use for the single-degree-of-freedom random oscillator given by (1.1) are described here. To keep a qualitative relevance to ship rolling in waves, the excitation of (1.1) is modeled as a linear function of wave slopes. The latter is computed from a spectral density of wave elevations, s_w, defined with the Bretschneider formula (following recommendations of the 15th International Towing Tank Conference in 1978):

$$s_w(\omega) = A\omega^{-5}\exp(-B\omega^{-4}), \quad \omega > 0, \tag{A.1}$$

where ω is a wave frequency. The parameters include $A = 173H_s^2T_1^{-4}$ and $B = 691T_1^{-4}$, where H_s is the significant wave height, i.e. twice the amplitude of the highest one-third of waves, and T_1 is the period corresponding to the mean frequency of waves.

Within the linear wave theory, the wave slope is expressed as the spatial derivative of wave elevation. Thus, the spectral density of wave slope angles, s_α, is given by

$$s_\alpha(\omega) = \left(\frac{\omega^2}{g}\right)^2 s_w(\omega), \quad \omega > 0, \tag{A.2}$$

where $g = 9.807$ m/s^2 is the gravitational acceleration and ω^2/g is the wave number or spatial frequency of linear waves.

Roll motions of a ship are excited by a moment of hydrodynamic pressure forces; neglecting effects of wave diffraction and radiation and expressing the moment in terms of angular acceleration, the spectral density is

$$s_y(\omega) = \omega_0^4 s_\alpha(\omega), \qquad \omega > 0, \tag{A.3}$$

where ω_0 is natural frequency of small undamped roll oscillations in calm water.

The range of ω is truncated to $0.65\omega_{\max} \le \omega \le 0.65\omega_{\max} + 2\omega_{\max}$, where $\omega_{\max}$ is the peak frequency. Throughout this paper, unless stated otherwise, the values taken are $H_s = 9$ m, $T_1 = 11.595$ s and $\omega_{\max} = 0.419$ rad/s. By convention, the autocovariance function $\gamma(t)$ is related to the spectral density through the Fourier transform as

$$\gamma(t) = \int_0^\infty s(\omega)\cos(\omega t)d\omega, \quad t \in \mathbb{R}. \tag{A.4}$$

Finally, the spectral density of the solution of the linear system (1.1) with $r(x) = \omega_0^2 x$ is given by

$$s_l(\omega) = \frac{s_y(\omega)}{(\omega_0^2 - \omega^2)^2 + (2\delta\omega)^2}, \quad \omega > 0. \tag{A.5}$$

Hence, the variance $\sigma_{\dot{x}}^2$ of the linear solution (i.e. below the "knuckle" point) can be computed as

$$\sigma_{\dot{x}}^2 = \int_0^\infty \omega^2 s_l(\omega)d\omega. \tag{A.6}$$

In (A.5) and (A.6), the damping parameter δ affects the oscillations of the system.

References

[1] A.A. Andronov, A.A. Vitt, S.E. Khaikin, Theory of Oscillators, Pergamon Press, 1966.

[2] V.L. Belenky, Piecewise linear approach to nonlinear ship dynamics, in: D. Vassalos, M. Hamamoto, A. Papanikolaou, D. Molyneux (Eds.), Contemporary Ideas on Ship Stability, Elsevier, 2000, pp. 149–160.

[3] V. Belenky, A capsizing probability computation method, J. Ship Res. 37 (3) (1993) 200–207.

[4] D. Paroka, N. Umeda, Capsizing probability prediction of the large passenger ship in irregular beam wind and waves: Comparison of analytical and numerical methods, J. Ship Res. 50 (4) (2006) 371–377.

[5] V. Belenky, K.M. Weems, W.M. Lin, Split-time method for estimation of probability of capsizing caused by pure loss of stability, Ocean Eng. 122 (2016) 333–343.

[6] E.V. Lewis (Ed.), Principles of Naval Architecture, SNAME, 1989.

[7] V. Belenky, K.M. Weems, C.C. Bassler, M.J. Dipper, B. Campbell, K. Spyrou, Approaches to rare events in stochastic dynamics of ships, Probab. Eng. Mech. 28 (2012) 30–38.

[8] G. Malara, P. Spanos, F. Arena, Maximum roll angle estimation of a ship in confused sea via quasi-deterministic approach, Probab. Eng. Mech. 35 (2014) 75–81.

[9] P. Anastopoulos, K. Spyrou, C. Bassler, V. Belenky, Towards an improved critical wave groups method for the probabilistic assessment of large ship motions in irregular sea, Probab. Eng. Mech. 44 (2016) 18–27.
[10] I.A. Kougioumtzoglou, P.D. Spanos, Stochastic response analysis of the softening duffing oscillator and ship capsizing probability determination via a numerical path integral approach, Probab. Eng. Mech. 35 (2014) 67–74.
[11] W. Chai, A. Naess, B.J. Leira, Stochastic nonlinear ship rolling in random beam seas by the path integration method, Probab. Eng. Mech. 44 (2016) 43–52.
[12] A. Reed, R. Beck, W. Belknap, Advances in predictive capability of ship dynamics in waves, in: 30th Symposium of Naval Hydrodynamics, Hobart, Australia, 2014.
[13] A. Reed, A. Zuzick, Direct assessment will require accreditation – what this means, in: 12th International Conference on the Stability of Ships and Ocean Vehicles, Glasgow, UK, 2015.
[14] J. Beirlant, Y. Goegebeur, J. Teugels, J. Segers, Statistics of Extremes, in: Wiley Series in Probability and Statistics, John Wiley & Sons, Ltd., Chichester, 2004, Theory and applications, With contributions from Daniel De Waal and Chris Ferro.
[15] S. Coles, An Introduction to Statistical Modeling of Extreme Values, in: Springer Series in Statistics, Springer-Verlag London Ltd., London, 2001.
[16] P. Embrechts, C. Klüppelberg, T. Mikosch, Modelling Extreme Events, Springer-Verlag, New York, 1997.
[17] A. Guha, A. Somayajula, J. Falzarano, Analysis of causeway ferry dynamics for safe operation of improved navy lighterage system, in: 13th International Ship Stability Workshop, Brest, France, 2013.
[18] B. Campbell, V. Belenky, V. Pipiras, Properties of the tail of envelope peaks and their use for the prediction of the probability of exceedance for ship motions in irregular waves, in: P. Spanos, G. Deodatis (Eds.), CSM7 Computational Stochastic Mechanics, Santorini, Greece, 2014.
[19] B. Campbell, V. Belenky, V. Pipiras, Application of the envelope peaks over threshold (epot) method for probabilistic assessment of dynamic stability, Ocean Eng. 120 (2016) 298–304.
[20] D. Glotzer, V. Pipiras, V. Belenky, B. Campbell, T. Smith, Confidence intervals for exceedance probabilities with application to extreme ship motions, REVSTAT 15 (2017) 537–563.
[21] V.L. Belenky, N.B. Sevastianov, Stability and Safety of Ships: Risk of Capsizing, The Society of Naval Architects and Marine Engineers, 2007.
[22] M.A. Mohamad, T.P. Sapsis, Probabilistic description of extreme events in intermittently unstable systems excited by correlated stochastic processes, SIAM/ASA J. Uncertain. Quantif. 3 (2015) 709–736.
[23] M.A. Mohamad, W. Cousins, T.P. Sapsis, A probabilistic decomposition-synthesis method for the quantification of rare events due to internal instabilities, J. Comput. Phys. 322 (2016) 288–308.
[24] M.A. Mohamad, T.P. Sapsis, Probabilistic response and rare events in Mathieus equation under correlated parametric excitation, Ocean Eng. 120 (2016) 289–297.
[25] V. Belenky, K. Weems, Probabilistic properties of parametric roll, in: T.I. Fossen, H. Nijmeijer (Eds.), Parametric Resonance in Dynamical Systems, Springer, 2011, pp. 129–146.
[26] V. Belenky, D. Glotzer, V. Pipiras, T. Sapsis, On the tail of nonlinear roll motions, in: 15th International Ship Stability Workshop, Stockholm, Sweden, 2016, pp. 109–114.
[27] M.R. Leadbetter, G. Lindgren, H. Rootzén, Extremes and Related Properties of Random Sequences and Processes, in: Springer Series in Statistics, Springer-Verlag, New York-Berlin, 1983.
[28] G. Lindgren, Stationary Stochastic Processes, in: Chapman & Hall/CRC Texts in Statistical Science Series, CRC Press, Boca Raton, FL, 2013, Theory and applications.
[29] J. Sólnes, Stochastic Processes and Random Vibrations: Theory and Practice, Wiley, 1997.
[30] V. Belenky, K.M. Weems, W.M. Lin, Numerical procedure for evaluation of capsizing probability with split time method, in: 27th Symposium on Naval Hydrodynamics, Seoul, Korea, 2008.
[31] A. Reed, Discussion to paper "numerical procedure for evaluation of capsizing probability with split time method", in: 27th Symposium on Naval Hydrodynamics, Seoul, Korea, 2008.
[32] K. Sobczyk, Stochastic Differential Equations, Kluwer Academic Publishers, Dordrecht, The Netherlands, 1991.
[33] T. Smith, A. Zuzick, Validation of statistical extrapolation methods for large motion prediction, in: 12th International Conference on the Stability of Ships and Ocean Vehicles, Glasgow, UK, 2015.
[34] M. St. Denis, W. Pierson, On the motions of ships in confused seas, in: SNAME Transactions, 1953.
[35] M. Longuet-Higgins, On the motions of ships in confused seas, Philos. Trans. Roy. Soc. Lond. Ser. A 249 (966) (1962) 321–387.
[36] P. Spanos, ARMA algorithms for ocean wave modeling, J. Energy Resour. Technol. 105 (1983) 300–309.
[37] A. Degtyarev, I. Gankevich, Hydrodynamic pressure under sea surface on basis of autoregressive model of irregular waves, Phys. Part. Nuclei Lett. 12 (3) (2015) 389–391.
[38] K. Weems, A. Reed, A. Degtyarev, I. Gankevich, Implementation of an autoregressive wave model in a numerical simulation code, in: 31st Symposium on Naval Hydrodynamics, Monterey, CA, USA, 2016.
[39] A. Degtyarev, A. Reed, Synoptic and short-term modeling of ocean waves, Int. Shipbuild. Prog. 60 (1–4) (2013) 523–553.